PERGAMON

Deep-Sea Research I 46 (1999) 1137–1160

DEEP-SEA RESEARCH
PART I

The onset of the Spring Bloom in the MEDOC area: mesoscale spatial variability

Marina Lévy*, Laurent Mémery, Gurvan Madec

Laboratoire d'Océanographie Dynamique et de Climatologie, Université Pierre et Marie Curie, 5, place Jussieu, 75252 Paris Cedex 05, France

Received 22 December 1997; received in revised form 9 June 1998; accepted 22 September 1998

Abstract

In the northwestern Mediterranean Sea, Coastal Zone Color Scanner images suggest that the eddies that participate in the restratification following deep convection interact with the spring phytoplankton bloom. The mechanisms for this interaction are studied using a biogeochemical model embedded in an eddy-resolving primitive equation ocean model. The model is initialized with a patch of dense water surrounded by a stratified ocean, which is characteristic of the winter situation. The atmospheric forcing is artificially held constant, in order to focus solely on the mesoscale variability. After a few days, meanders develop at the periphery of the patch, inducing its sinking and spreading. Mesoscale upward motions are responsible for the shoaling of the mixing layer in the trough of the meanders. As sunlight is the main factor regulating primary production at this time of year, this shoaling increases the mean exposure time of the phytoplankton cells and thus enhances productivity. Consequently, the majority of phytoplankton production is obtained at the edge of the patch, in agreement with in situ data. Through advection, phytoplankton is then subducted from these sources towards the crest of the meanders. Our results suggest that this mesoscale transport is responsible for a decorrelation between phytoplankton biomass and primary production.

1. Introduction

In temperate regions of the ocean, phytoplankton concentrations show strong seasonal variability. These regions are characterized by deep winter vertical mixing, with very low phytoplankton biomasses within a nutrient-rich euphotic layer. As

* Corresponding author. Fax.: 00 33 1 44 27 71 59; e-mail: marina@lodyc.jussieu.fr

0967-0637/99/$ – see front matter
PII: S0967-0637(98)00105-8

phytoplankton growth is mainly dependent on the availability of light and dissolved mineral nutrients, this winter regime is due to the dispersion of the phytoplankton cells within a mixed layer considerably deeper than the euphotic layer (Riley, 1942; Sverdrup, 1953). As the year progresses, the surface layer becomes more stable, thus allowing the nutrients entrained during winter to be utilized continuously. As a consequence, there is a bloom of phytoplankton. Nutrients start to be limiting at the end of the bloom, when they become depleted from the surface.

This classical, seasonal and regional scenario is, however, strongly modulated by temporal and spatial signals of smaller scale (Watson et al., 1991; Robinson et al., 1993; Yoder et al., 1993). These smaller-scale phenomena can be responsible for variability in primary production whose amplitude can match that of the larger scale variability. Time variability in phytoplankton concentrations during a bloom can to a great extent be attributed to the variability of the atmospheric forcing. The mean trend of this forcing is responsible for the mean seasonal variability: stratification of the water column – and thus the spring bloom – starts as soon as the net heat flux at the sea surface becomes positive. Higher frequency atmospheric events (from one to a few days), such as wind bursts, are sufficient to destroy the stratification and temporarily interrupt the bloom. On the other hand, spatial variability in phytoplankton distribution results mainly from the variability in the three-dimensional ocean circulation; firstly, because the distribution of biogenic material is continually rearranged by transport processes; secondly, because ocean circulation can affect primary production by modulating in situ growth rate. This can be done either by modulating the mixing layer depth and thus the amount of light incident on a cell, or by affecting the concentration of nutrients. Vertical velocities associated with mesoscale instabilities can reach a few tens of meters per day (Pollard and Regier, 1990), while phytoplankton growth occurs within a couple of days in a layer no deeper than a hundred meters. Therefore, movements generated by mesoscale dynamics are very likely to strongly modify phytoplankton growth.

There have been several studies in recent years to understand the interaction between primary productivity and mesoscale physics within idealized frameworks. These studies have shown that a number of these processes are based on the fertilizing effect of the vertical velocities associated with specific mesoscale features, such as a meandering current (Flierl and Davis, 1993; Dadou et al., 1996), a coastal transition zone (Moisan et al., 1996), a turbulent eddy field (McGillicuddy and Robinson, 1997), an isolated eddy (McGillicuddy et al., 1995), eddy–eddy interactions (Yoshimori and Kishi, 1994) and frontal zones (Smith et al., 1996; Spall, 1998). Most of these studies are based on quasi-geostrophic physics and support the principle of a strong influence of mesoscale dynamics on primary productivity. However, some studies conclude that there is a weaker effect (Dadou et al., 1996; Smith et al., 1996), which could be due to the strong underestimation of vertical velocities in quasi-geostrophic models.

Within this context, this is the first of two papers dedicated to understanding the observed variability during the onset of the spring bloom in the northwestern Mediterranean sea (MEDOC area). This region is typical of temperate regions, with the

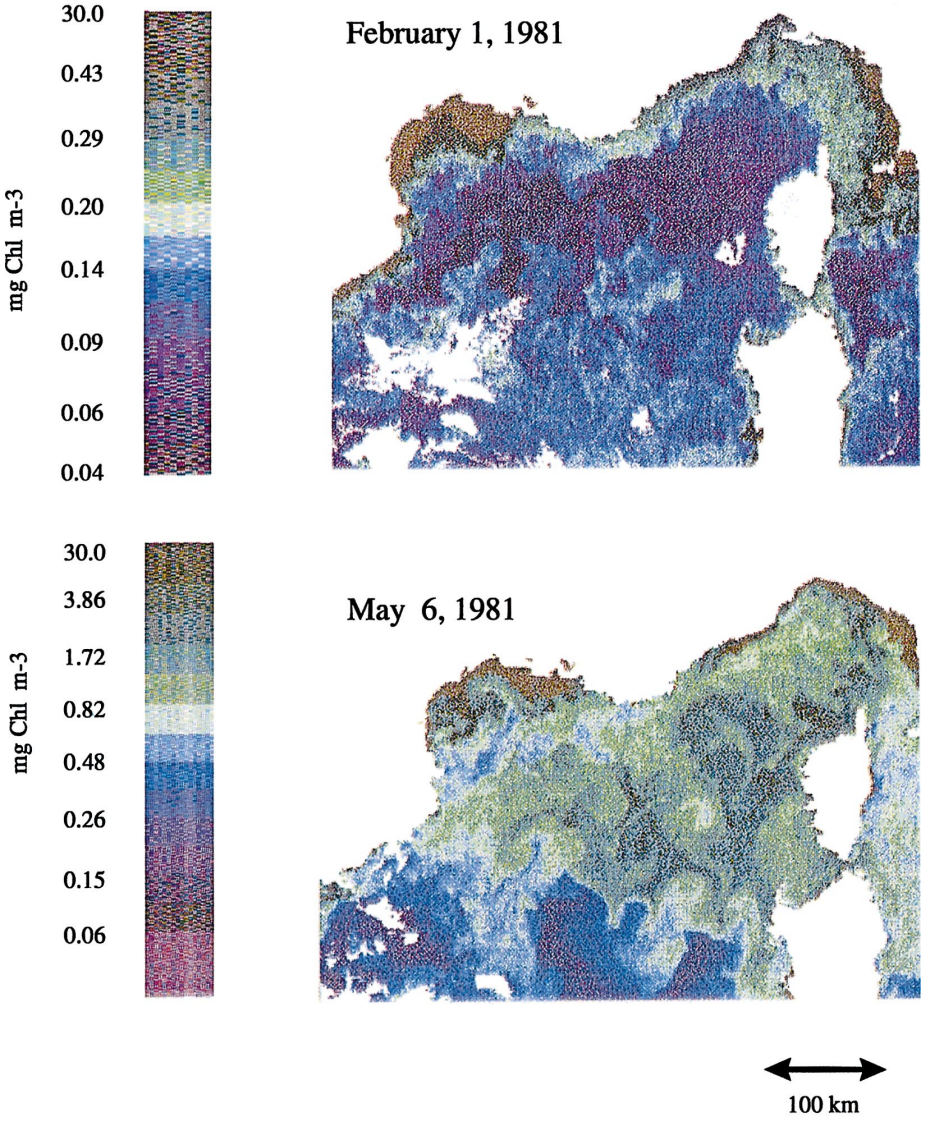

Fig. 1. CZCS images over the MEDOC area in February and May 1981 (from Morel and André, 1991) These images show the surface chlorophyll concentrations, and can be interpreted as phytoplankton concentrations. They illustrate the mean trend of the bloom, with minimum phytoplankton concentrations in winter (February image), and high concentrations during spring (May image). The mesoscale signature on phytoplankton is obvious on both images, suggesting strong interactions between the oceanic mesoscale dynamics and phytoplankton dynamics during the onset of the bloom.

advantage that is has been the subject of numerous studies concerning its physics, biology and geochemistry. In addition, the cloud cover is rather weak, even during winter, which guarantees high quality of remote-sensing images of ocean color. Coastal Zone Color Scanner (CZCS) images (André, 1990; Morel and André, 1991) have revealed phytoplankton heterogeneity at scales similar to mesoscale eddies over this area during winter and spring (Fig. 1). This first paper more specifically aims at understanding the processes responsible for this observed mesoscale spatial variability, during the onset of the bloom, when nutrients are still plentiful. The companion paper (submitted) complements this approach, in a study that combines mesoscale spatial variability with high-frequency temporal variability, and investigates the decay of the bloom when nutrients become depleted.

The MEDOC region is the location of intense mesoscale activity, associated with the process of deep-water formation. It is subjected to strong wind bursts during winter and spring (Mistral, Tramontane), associated with intense cooling. During winter, a deep-mixed patch of dense water (called "chimney" earlier: Killworth, 1976) is formed, which sometimes extends from the surface down to the ocean bottom (Medoc group, 1970; Leaman and Schott, 1987). Therefore, water in this patch is rich in nutrients (Coste et al., 1972). The breakup (or sinking and spreading) of the patch, associated with a rapid restratification of the surface waters, involves mesoscale eddies, which have the scale of the first Rossby radius of the surrounding area ($\sim$ 5–10 km, Gascard, 1978; Gaillard et al., 1997). These eddies are attributed to baroclinic instability and are responsible for the redistribution of water masses (Killworth, 1976; Gascard, 1978; Madec et al., 1991a) As expected, restratification causes the onset of the bloom (Jacques et al., 1973), and eddies involved in it are very likely responsible for the observed mesoscale variability in the phytoplankton field (André, 1990; Morel and André, 1991).

In order to assess the role of these baroclinic eddies with regards to the phytoplankton distribution, a numerical model is employed, namely a primitive equation dynamical model, which has an explicit mixed-layer representation and an embedded primary production model. As our focus here is solely on mesoscale variability, the atmospheric forcing is artificially held constant. In a previous study (Lévy et al., 1998a), the importance of mesoscale processes for predicting primary production was examined for a similar scenario; by performing two experiments, one explicitly resolving the mesoscale, the other parameterizing mesoscale transfers by using an horizontal diffusion operator, it was shown that primary productivity could be underestimated by up to a factor of four when mesoscale eddies were not explicitly simulated. In view of the tremendous importance of mesoscale eddies in the MEDOC area emphasized by these results, the eddy resolving experiment is explored in more detail, and the processes involved in the interaction between phytoplankton and mesoscale dynamics are examined.

The paper is organized as follows: first, the model and the initial conditions are presented. The specific oceanic mesoscale variability we are interested in is then described, and the response of the biology to this mesoscale variability is discussed. Finally, we diagnose the simulated variability of phytoplankton fields by looking at the different forcing mechanisms and compare our simulation to observations.

2. Model description and initial conditions

The primitive equation model OPA (Madec et al., 1991a; Delecluse et al., 1993) is used to simulate the sinking and spreading phase that follows deep convection. Vertical eddy coefficients are computed from an embedded 1.5 turbulent closure model (Blanke and Delecluse, 1993) based on a prognostic equation for the turbulent kinetic energy and a diagnostic computation of the mixing length. Cut-offs are applied on the diffusivity and viscosity coefficients to avoid numerical instabilities associated with too weak vertical diffusion (set to 10^{-5} and $10^{-6}\,m^2\,s^{-1}$, respectively). This closure allows us to deal with statically unstable density profiles, as it leads to large values of diffusivity (up to $1\,m^2\,s^{-1}$), which restore the static stability of the water column. A closed domain is initialized with a preformed patch of dense water (Fig. 2a), whose main characteristics (density, density gradients, size) are in agreement with in situ observations (Fig. 2b). The first three Rossby deformation radii of the stratified waters surrounding the patch are 8.4, 3.8 and 2.5 km. In order to resolve baroclinic mesoscale eddies, the horizontal grid spacing is uniformly set to 2.5 km (on a C-grid). In order to insure numerical stability, weak horizontal mixing of density and momentum is included through biharmonic friction terms that selectively dissipate the smallest horizontal scales of each field. A constant biharmonic coefficient was chosen for all quantities, $-0.32\times10^{9}\,m^4s^{-1}$. The model has 20 vertical layers, with thicknesses varying from 10 to 25 m in the upper 130 m to 500 m near the ocean bottom. The initial velocity field is in geostrophic balance, in order to minimize the excitation of inertial waves. The time step is 8 min.

No-slip conditions and no heat flux are applied along solid boundaries. At the sea surface, we assume a zero wind stress and a zero net heat flux, held constant in time and space. Therefore, the ensuing ocean circulation results only from the imposed initial conditions, which provide plentiful available potential energy. The surface heat flux is split up into a penetrative part $Q_{sol}=150\,W\,m^{-2}$ (corresponding to the incoming solar radiation), exactly compensated by the non-penetrative part (corresponding to the sum of the latent, sensible and infra-red fluxes). A formulation including extinction coefficients is assumed for the downward irradiance I (Blanke and Delecluse, 1993):

$$I(z)=Q_{sol}(R\exp(-z/\xi_1)+(1-R)\exp(-z/\xi_2)) \tag{1}$$

with $\xi_1=0.35$ m, $\xi_2=23$ m and $R=0.58$. This heat forcing is responsible for the generation of static instabilities (and is therefore an important source of vertical mixing) as the penetration of the solar heat flux causes heating of the first few layers while only the very first layer is cooled. A linear equation of state is assumed, specific to the conditions of the northwestern Mediterranean sea (T in degrees Celsius):

$$\rho=1050.29-1.615\,T. \tag{2}$$

A primary production model is embedded on-line within OPA. This model is a simplified version of the biogeochemical model developed in a one-dimensional

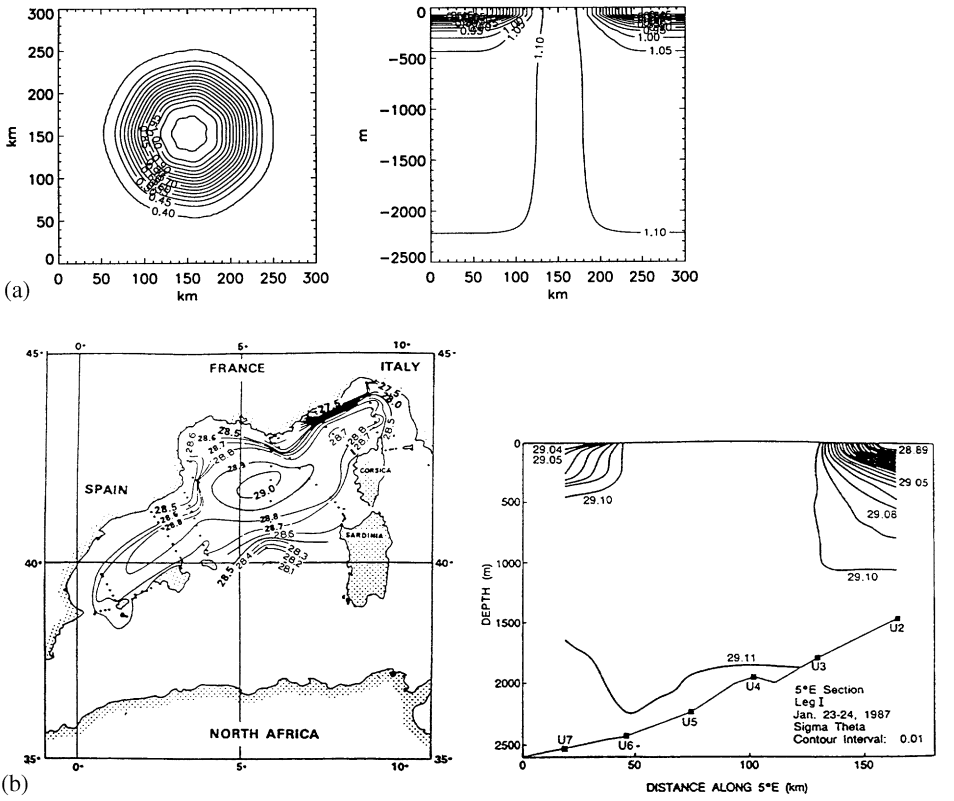

Fig. 2. (a) Initial density field, relatively to $\sigma_\theta = 28.0$. Left: surface horizontal section. Right: vertical section at the center of the domain along $y = 150$ km. The domain is a closed, flat basin on a β-plane of 300 km × 300 km × 2500 m centered at 42°N. An homogeneous chimney of dense water ($\sigma_\theta = 29.1$) is set in a patch of about 20 km radius in the center of the domain, perturbed with a sinusoid of mode seven and 1 km in amplitude. Outside the patch, density is relaxed to a background stratification, within a horizontal gradient area of 80 km. The mean diameter of the chimney is therefore 70 km. The background density profile is homogeneous over the first 80 m. (b) Left: winter sea surface density, from the Elie Monnier cruise (Feb–Mar 1969). Right: vertical section of density along 5°E, from Leaman and Schott (1987), showing a column of dense water ($\sigma_\theta = 29.1$) extending from the surface to the ocean bottom. The diameter of this column is 87 km.

vertical study by Lévy et al. (1998b) for the northwestern Mediterranean seasonal cycle of primary production and export fluxes. It consists of four prognostic variables, expressed in terms of their nitrogen content: nutrients (N), phytoplankton (P), zooplankton (Z) and detritus (D) (Fig. 3). This simplicity is justified by the very short period of interest (less than one month) and the characteristics of the trophic web during that period (new production, weak regeneration, weak grazing) (Lévy et al., 1998b). The complete description of this NPZD biogeochemical model is given in the appendix.

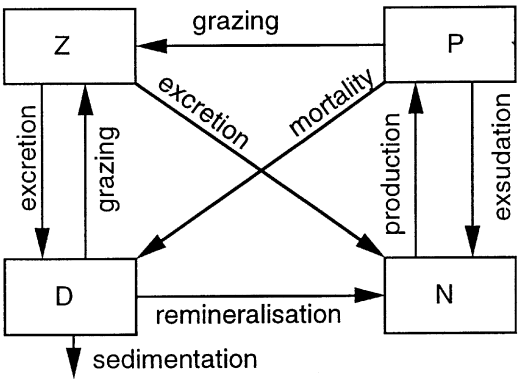

Fig. 3. Schematic representation of the "NPZD" biogeochemical model (N: nutrients, P: phytoplankton, Z: zooplankton, D: detritus).

The Eulerian time evolution of any of the four state variable concentrations C is controlled by biogeochemical processes (through a source/sink function S), advection and vertical diffusion:

$$\frac{\partial C}{\partial t} = S(C) - \nabla.(UC) + \frac{\partial}{\partial z}\left(k_z \frac{\partial C}{\partial z}\right) \tag{3}$$

where U and k_z are the velocity vector and the diffusion coefficient computed by the physical model. A positive-definite transport scheme (Smolarkiewicz and Clark, 1986) is used for the advection of biological tracers. This scheme is slightly diffusive; therefore, no additional horizontal diffusion is needed to insure the numerical stability of the system.

Initialization of the biogeochemical variables is done after a spin up of eight days for the circulation fields. As suggested by observations (Coste et al., 1972; Jacques et al., 1973), initial nitrate and phytoplankton concentrations are chosen to be proportional to density. High densities are correlated with high nitrate and low phytoplankton concentrations. Zooplankton and detritus are uniformly set to low values, 0.015 and 0.1 mmol m^{-3}, respectively.

3. The oceanic mesoscale variability

The main features of the breakup of a convective dense-water patch are well known. These features have been investigated in a modelling study using a fine-scale version of OPA (Madec et al., 1991b): the release of the available potential energy contained within the dense-water patch occurs through the development of mixed barotropic–baroclinic instability. These instabilities emerge at the rim of the patch and work as a vehicle for the transfer of water masses. Important vertical velocities are associated with this transfer (typically, tens of meter per day) and modify the thermal

structure. The dense waters sink to the bottom, whereas the surface of the patch is covered with peripheral lighter waters. In the following section, the sinking and spreading of the dense-water patch achieved through these mesoscale transfers is presented in more detail. Particular attention is paid to the factors likely to affect the biogeochemical system: the generated circulation, which rearranges the phytoplankton distribution and can bring nutrients into the euphotic layer, and the mixing layer depth, which modulates the in situ growth rates of phytoplankton.

After a few days of model simulation, the signature of the instabilities starts appearing in the surface density field in the form of meanders along the front that defines the neutrally stable column (Fig. 4). Fourteen small meanders start to develop at the outer edge of the convective region (days 4–12), with a corresponding wavelength of $\sim$15–30 km. In that sense, they can be attributed to the second and third radii of deformation of the initial state. After 16 days the mode with fourteen

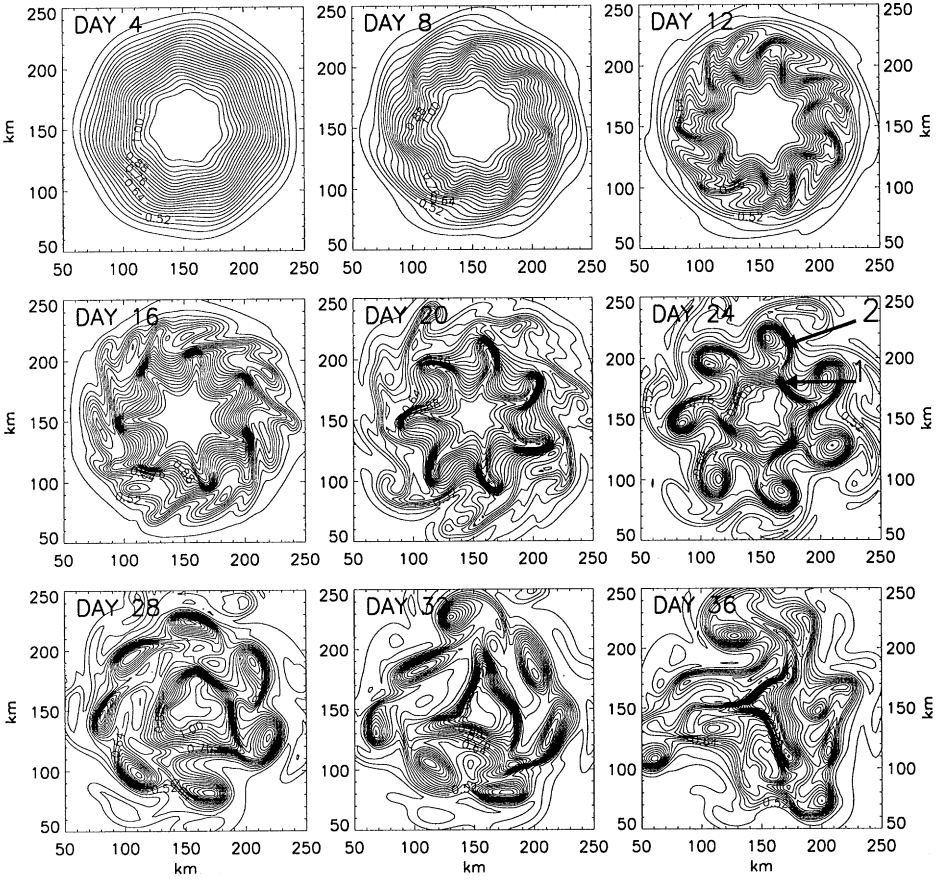

Fig. 4. Time series of the surface density field (relatively to $\sigma_\theta = 28.0$). Contour interval is 0.03 in units of σ_θ. Only a zoom of the domain is represented. The arrows at day 24 indicate the location of stations 1 and 2.

meanders has almost vanished, and seven meanders of ~ 50 km wavelength are more pronounced. This wavelength corresponds to the first baroclinic mode. Similar meanders have been observed by in situ measurements (Gascard, 1978; Gaillard et al., 1997). Meanders grow from days 12 to 24, after which they break into seven cyclonic eddies between days 20 and 24, while the front surrounding the dense-water patch is propagating towards the center. After day 24, eddies start evolving towards an ellipsoidal shape and separate from the central structure. Between days 28 and 32, symmetrical properties are lost as eddies propagate westward in response to the β-effect. After day 32, eddies start collapsing themselves, while cascading towards greater scales. Note that mode fourteen and mode seven meanders lean in opposite directions, suggesting that the underlying instabilities are of different nature (i.e. mainly barotropic or mainly baroclinic (Pedlosky, 1987). Fig. 4 also shows the progressive overlapping of the central convective area by lighter waters. The mean effect of the instabilities is to collapse the dense-water patch, and therefore to stabilize the system.

The three-dimensional circulation is tackled using the numerical tool developed by Blanke and Raynaud (1997), which enables one to compute individual parcel trajectories from a stationary velocity field. For instance, Fig. 5 shows six different trajectories at day 16, integrated for 8 days, and all starting on the same radial road at 30 m depth. They illustrate a cyclonic circulation around the dense-water patch, following the shape of the isopycnals; trajectories tend to sink when they are directed outward (in the upstream side of the density meanders), and to rise towards the surface in the opposite case (downstream), in good agreement with the baroclinic instability theory: the denser waters sink out of the convective area, while the lighter peripheral water masses are advected up towards the center. A parcel is transported from one meander to the next in about four days, which corresponds to twenty eight days for a complete tour. Important vertical excursions are also evidenced, which can exceed 100 m in a couple of days (Fig. 5), in agreement with observations (Gascard, 1978).

As expected from the quasigeostrophic study of Klein and Hua (1988), this mesoscale flow has a large impact on the mixing layer (Fig. 6). The mixing layer is initially uniformly set to 80 m depth, which corresponds to the top of the thermocline in the stratified zone. Because there is no wind, the main source of vertical turbulence at the surface is the penetration of radiative heat flux: it causes heating of the first few layers while only the very first layer is cooled, and is thus responsible for the generation of static instabilities, and consequently for vertical mixing. Therefore, after a few days (before the biological model is activated), the mixing layer reaches the bottom within the convective area, where there is no stratification. In the background zone, it keeps its initial depth, since it is bounded by the thermocline. In the frontal zone around the patch, mesoscale features strongly affect the mixing-layer depth. At day 8, the mixing layer has shoaled on the downstream side of the fourteen density crests of the meanders. On day 16, instabilities of mode seven are preponderant, and mixing-layer depth variability reaches its maximal amplitude, with values up to 2500 m in the central zone, to 80 m in the background stratified zone, and varying between 20 and 80 m in the meander zone. Minima of mixing-layer depth appear in a surface density trough, where vertical velocities are directed upward. Relative maxima appear at density crests, where vertical velocities are directed downward. Between days 16 and 24,

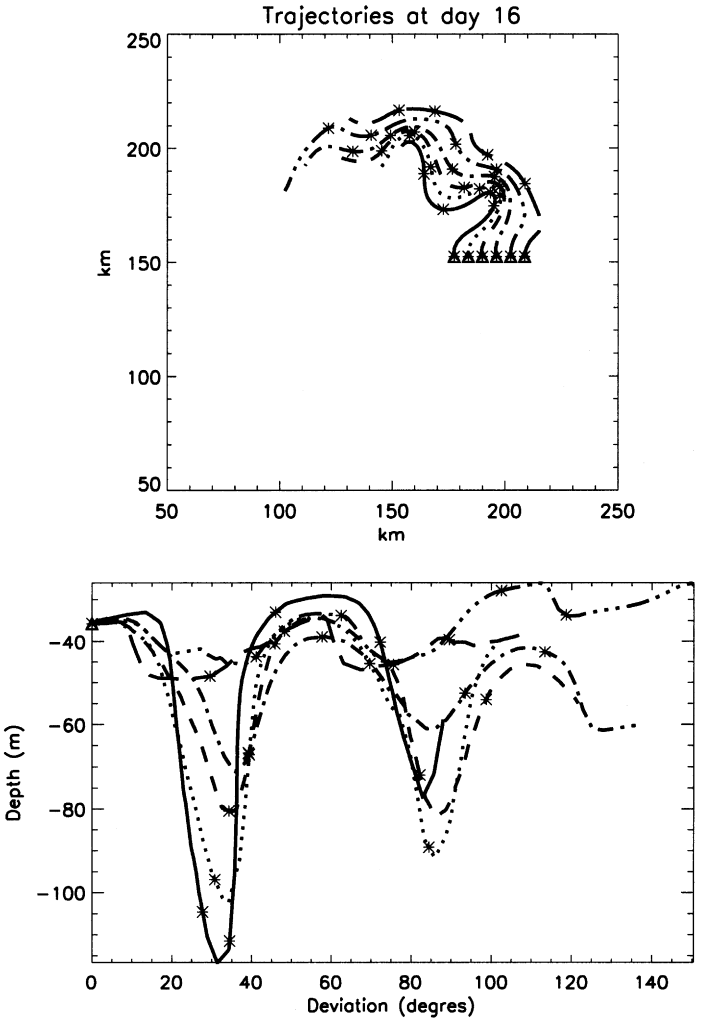

Fig. 5. Six trajectories computed with the velocity field at day 16, and integrated for 8 days. Triangles indicate their initial positions. Each trajectory is represented twice, using the same linestyle. On the top figure, trajectories are projected on the horizontal. On the bottom figure, they are projected on the surface defined by the vertical and by a circle centered at the center of the chimney (deviation is counted anti-clockwise starting from the initial deviation). Stars give an indication of the time scale: two stars are separated by one day.

this correlation between ascendant movements and mixing-layer depth minima remains apparent at the very border of the convective zone. Then, when eddies are generated and separate from one another, a zone of shallow mixing is associated with each of them (day 28). These zones appear along the front defined by the isopycnals separating two eddies, in upward velocity cells. In the center of the basin, an important zone of shallow mixing develops, as the surface layers of the convective area get progressively stratified.

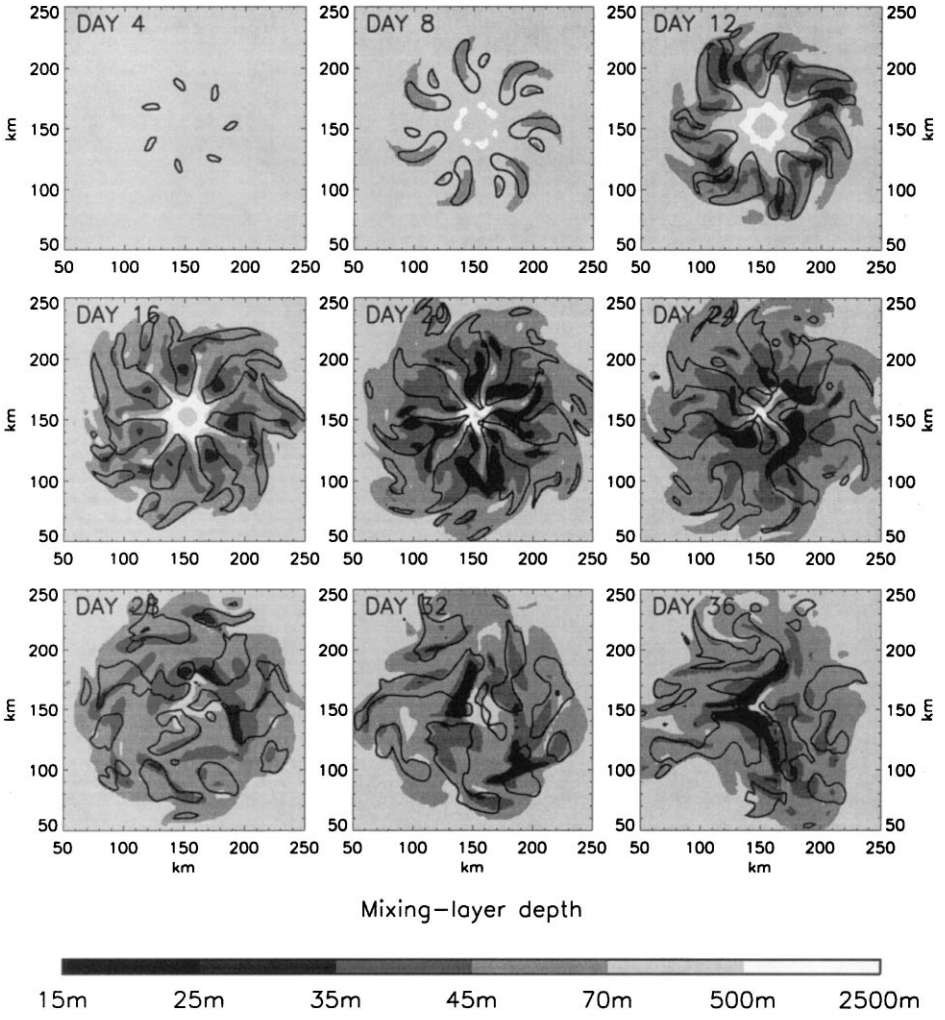

Fig. 6. Mixing-layer depth time series. The mixing layer is defined as the surface layer where the vertical mixing coefficient is greater than $10^{-4}\,m^2\,s^{-1}$. As this coefficient exhibits a sharp vertical variation at the bottom of the mixing layer, this definition is quite insensitive to the minimum value chosen, as long as it is reasonable (between 5×10^{-4} and $5\times10^{-3}\,m^2\,s^{-1}$). Contoured areas show the location where vertical velocities are directed upward.

4. The response of the biology

4.1. Primary productivity

During deep convection, vertical mixing insures a perfect enrichment of the euphotic layer in nutrients. However, primary productivity is strongly inhibited because

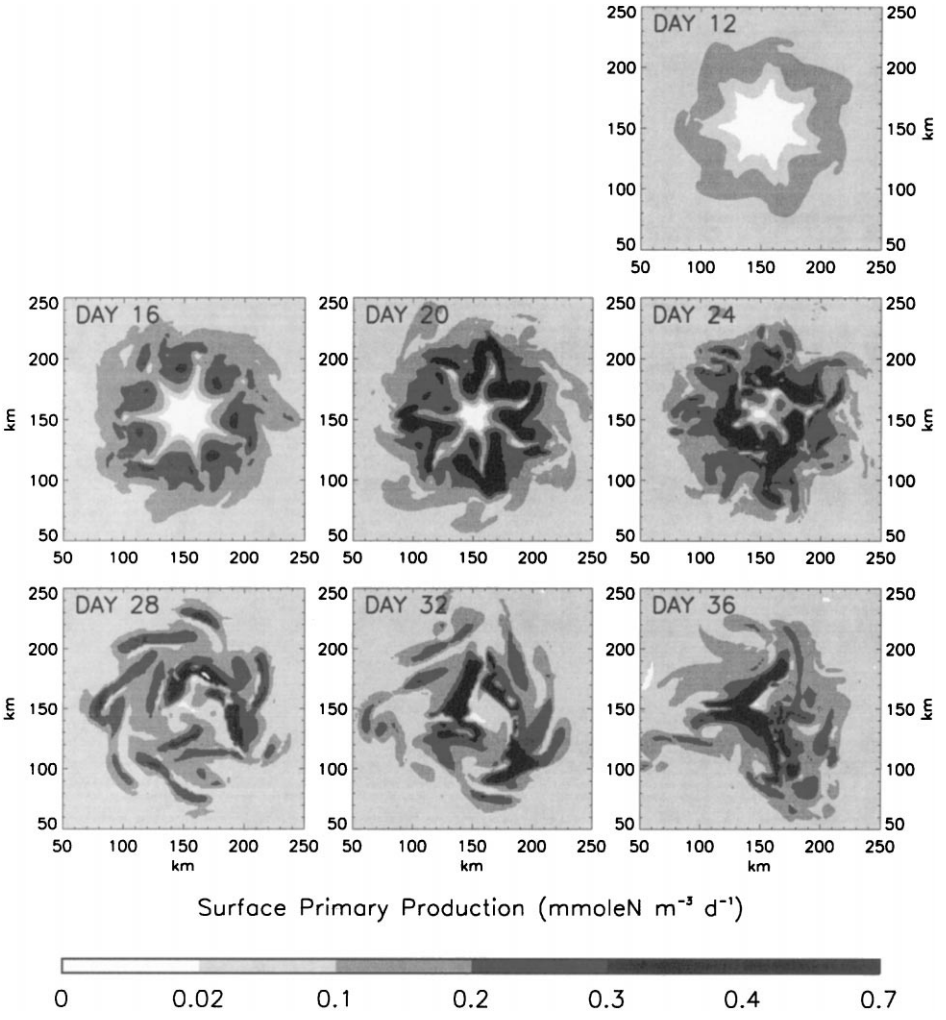

Fig. 7. Surface primary production time series.

phytoplankton cells are dispersed in a mixing layer deeper than the euphotic layer. In such a situation, the stabilization of the water column (in other words the shallowing of the mixing layer) is the necessary condition for phytoplankton growth (Riley, 1942). In our simulation, nutrients never become depleted at the surface (not shown). Therefore, primary production is mainly controlled by the availability of light, and thus strongly affected by the mixing-layer depth.

A time series of the simulated surface primary production is shown in Fig. 7. As expected, primary productivity is very weak ($\leqslant 0.02$ mmol N m^{-3} d^{-1}) in the convective area, where very deep vertical mixing strongly inhibits photosynthesis. In the region of the instabilities, surface primary productivity is maximum and shows large

mesoscale variability. Maximum values increase with time from day 12 to day 20, when they reach up to 0.7 mmol N $m^{-3} d^{-1}$. Away from the center, primary production is low ($\leqslant 0.1$ mmol N $m^{-3} d^{-1}$) and spatially homogeneous. By comparing Figs. 6 and 7, it appears that, as expected, spatial variability of primary productivity is very closely related to the variability of the mixing-layer depth field. In particular, maxima of primary productivity are located precisely in areas where the mixing layer is shallowest, for instance in the trough of the meanders at day 16, and along the eddies at day 28. Moreover, the central area of very low productivity diminishes with time, as the domain becomes progressively restratified, and has almost completely disappeared by day 24. In the background, the mixing layer remains at a constant depth of 80 m, which explains the low and homogeneous productivity. Depth-integrated primary production over the first 100 m shows almost the same spatial variability as surface primary production (not shown), indicating there is no significant productivity below the mixing layer.

4.2. *Phytoplankton distribution*

A time series of surface phytoplankton surface concentrations is shown in Fig. 8. As for primary productivity, phytoplankton concentrations are minimum in the center of the convective area ($< 10^{-2}$ mmol N m^{-3}) and are small and homogeneous (0.3 mmol N m^{-3}) in the background. In the instability area, phytoplankton develops in a heterogeneous manner, and its surface distribution shows mesoscale features whose scale and shape and reminiscent of the surface density field. At days 16, seven zones of maximum phytoplankton concentrations appear in the meander trough and can be viewed as the signature of the instabilities of mode seven. By day 24, maximum concentrations reach 1 mmol N m^{-3}. They stay located within the eddies, as well as in a narrow area (about 20 km wide) just around the convective area. Therefore, strong horizontal concentration gradients appear between the convective area and its periphery. However, the spatial variability in the phytoplankton surface field is somehow different than that of the primary productivity surface field. This is particularly clear at day 24, where primary productivity shows high values confined just at the border of the convective area, while the phytoplankton distribution follows the shape of the isopycnals.

Unlike the case for primary production, depth-integrated phytoplankton distributions over the first 100 m show different characteristics than surface concentrations (Fig. 9). In particular, the signature of the instabilities of mode 14 appears clearly in the depth integrated field at day 16 in the form of bent filaments of biomass, while it has disappeared from the surface field. This indicates that the instabilities of mode 14, whose development occurs faster than that of mode seven, has led to a production of phytoplankton that has rapidly been exported in subsurface. After day 24, while surface biomass maxima are found around the convective area (Fig. 8), depth integrated maxima are located in the branches of the instabilities (Fig. 9). This seems to indicate that phytoplankton develops at the surface in the meander trough, and is then subducted through the instabilities toward the crests, still developing, but at a lower rate. This route is coherent with that diagnosed from the cell trajectories (Fig. 5):

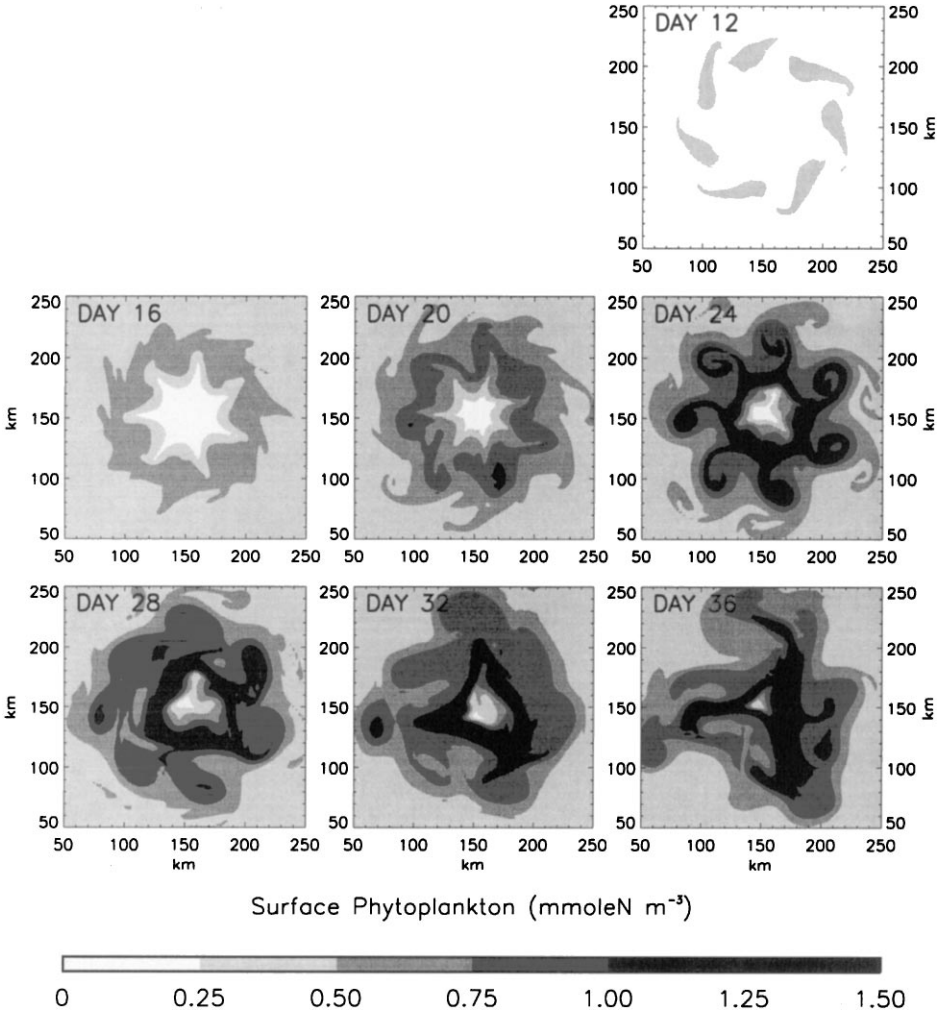

Fig. 8. Surface phytoplankton concentration time series.

it takes only a couple of days for a cell to be transported down to a 100 m depth, on its way from the trough to the crest of an instability. Phytoplankton decay by mortality (~ 30 d) being much slower, this scenario is also realistic. It is investigated further in the following.

5. Analysis of phytoplankton forcing terms

The two main factors regulating phytoplankton distributions are primary productivity and transport processes. Indeed, the grazing pressure on phytoplankton is very

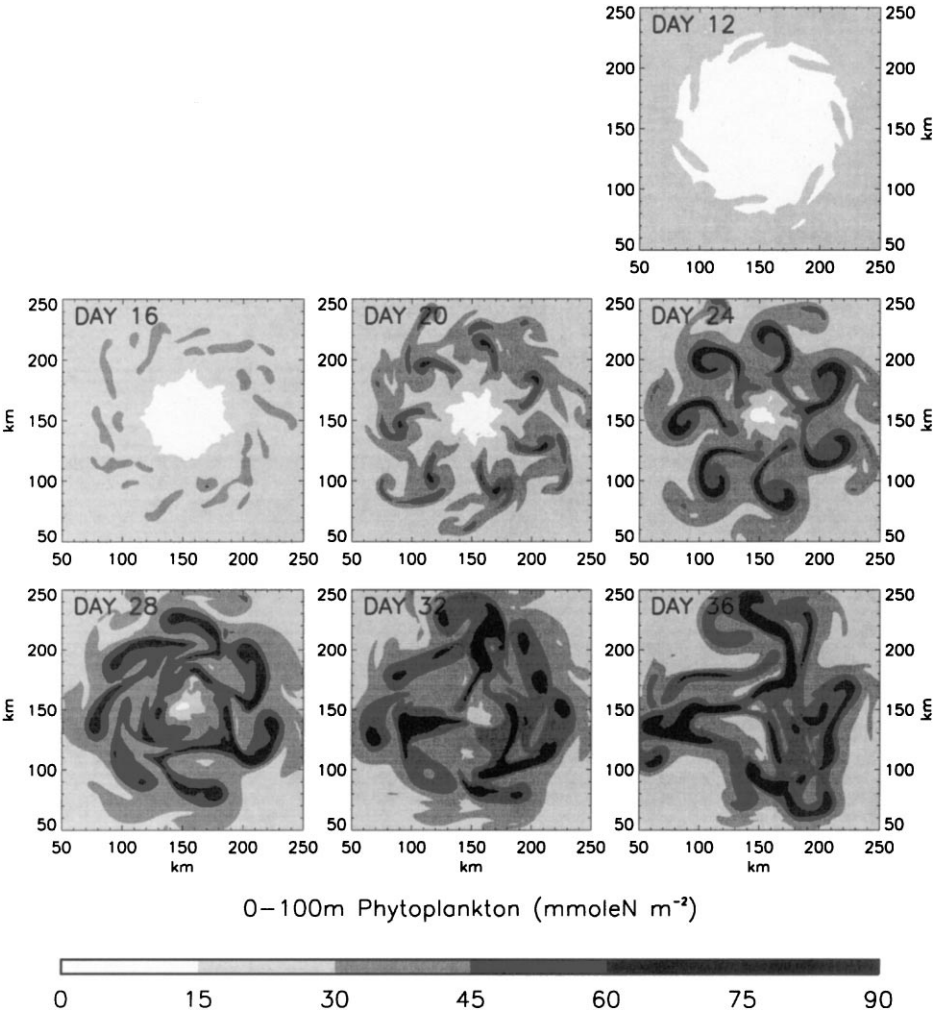

Fig. 9. Time series of phytoplankton concentration integrated over the first 100 m.

low, as zooplankton start to grow only at the end of the simulation (not shown). Field observations (Nival et al., 1975) and one-dimensional model results (Lévy et al., 1997b) provide evidence that zooplankton develops only a month after the beginning of the bloom in the MEDOC area, which gives us confidence in this result.

In order to explain the decoupling between the spatial variability of primary production and phytoplankton, the relative strength of transport and production with regards to phytoplankton distribution is assessed. This is done by comparing the different terms in the phytoplankton equation (time derivative, production, grazing, mortality, vertical diffusion, advection, Eq. (3)). Two specific fixed stations are chosen for that purpose, located in key areas of the domain at day 24 (see the arrows on

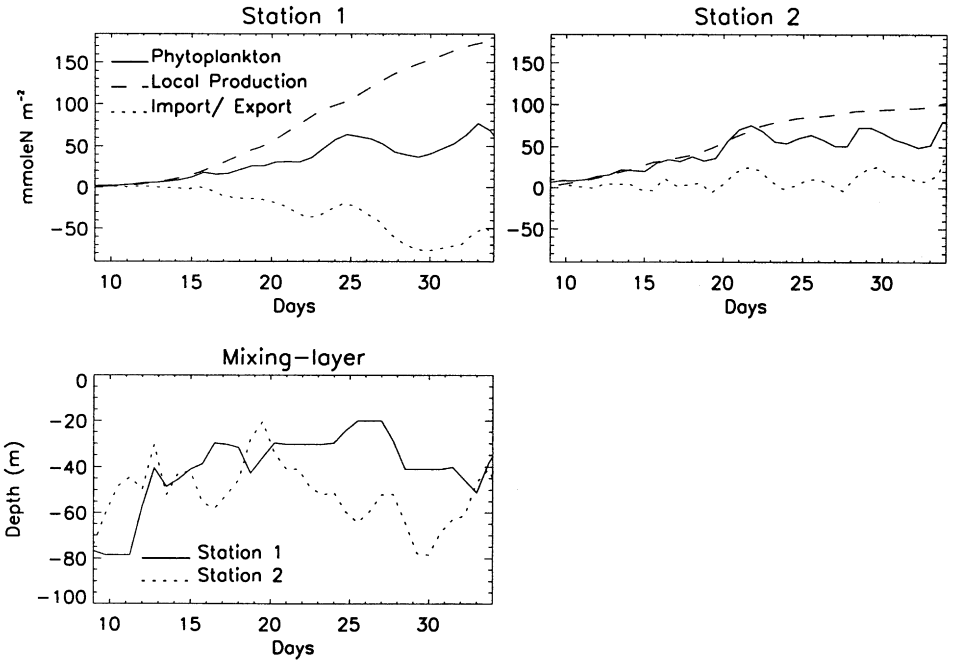

Fig. 10. At stations 1 and 2 (indicated by the arrows in Fig. 4), production and advection of phytoplankton integrated over the first hundred meters of the water column and integrated over time (and therefore in units of phytoplankton concentration per square meter). Time-integrated production represents the amount of phytoplankton that is locally produced (Local Production), whereas time-integrated advection represents the amount of phytoplankton that is imported or exported from the station (import/export). They are compared to total depth-integrated phytoplankton stock. Bottom figure shows the time evolution of the mixing-layer depth at stations 1 and 2.

Fig. 4): station 1 is located in a meander trough; station 2 is located within the upstream side of the corresponding crest. The characteristics at these locations do not change much over the course of the simulation due to the slow propagation of the instabilities. Both stations are characterized by high integrated phytoplankton concentrations (Fig. 9). Production and advection are integrated over the first hundred meters of the water column and integrated over time (Fig. 10). Therefore, they are equivalent to a phytoplankton concentration per square meter. Time-integrated production represents the amount of phytoplankton that is locally produced, whereas time-integrated advection represents the amount of phytoplankton that is imported or exported from the station. Their sum almost equals the total phytoplankton concentration, as the other terms in the equation (grazing, mortality, and depth integrated vertical mixing) are negligible.

Station 1 is characterized by a shallow mixing layer (less than 50 m after day 13, Fig. 10). Therefore, at station 1, production is favored, and local production is high.

Station 1 is also characterized by strong losses of biomass through advective export, which account for about half of the local production. At station 2, the mixing layer is often deeper, and local production is about twice as small as at station 1 (Fig. 10); some phytoplankton is imported, which contributes to an increase in the total local stock and therefore sustains production. Finally, depth integrated phytoplankton concentrations are similar at stations 1 and 2, even though production rates differ by a factor two. This analysis emphasizes the strong decorrelation that exists between productive areas and biomass-rich areas. Production mainly occurs in the meander trough, around the convective area, within a shallow mixing layer. Then, as previously hypothesized, the phytoplankton cells are transported from this area toward the meander crests. This transport is achieved in a couple of days. It follows the water mass circulation: phytoplankton is indeed subducted from point 1 at the surface to point 2 at depth, which explains the differences between surface and depth-integrated phytoplankton distributions.

6. Comparison with data

This study is idealized, as the problem is artificially symmetric and the forcing is constant over time and space. However, the dynamics of the collapse of the dense-water patch and of the associated instabilities are a crucial factor during this period. It is therefore possible to simulate the main characteristics of the observed phytoplankton fields, and in particular the right spatial scales of variability. However, one should keep in mind that the simulated situation corresponds to a zero net heat flux, which in the real world happens only during transient periods. Therefore, the temporal scales of variability, due both to the progressive spring warming and to higher frequency events (such as wind bursts), cannot be assessed in this simulation. Seasonal variability as well as smaller time scale variability are investigated in the companion paper, where variability in the atmospheric forcing is taken into account.

Intensive winter and spring surveys of hydrological as well as biological parameters were carried out in the MEDOC area in the seventies during the Mediprod cruises (Coste et al., 1972; Nival et al., 1972; Jacques et al., 1973). The sampling resolution of these data is clearly coarser than the mesoscale, but they bring interesting insights on the mean phytoplankton distribution. Three areas have been identified from the Toulon-Barcelona transect of Mediprod II (Fig. 11a): a turbulent area characterized by low phytoplankton biomasses (stations 2 and 3); a more stable area where higher concentrations of phytoplankton develop thanks to stratification (station 4); a transient area in between (station 5), where maximum chlorophyll concentrations are found. Model results reproduce this general pattern (Fig. 11b): the concentrations of phytoplankton averaged around the center are maximum at the border of the convective area; the value of this maximum is the same ($\sim 1.5\ \mathrm{mg\,Chl\,m^{-3}}$), and so is its vertical extend (~ 30 m). The main difference between the model results and the data is the distance of this maximum from the center of the convective region, which is approximately two to three times smaller in the model. However, this difference can easily be explained by looking at Fig. 2: the real problem indeed does not show a circular

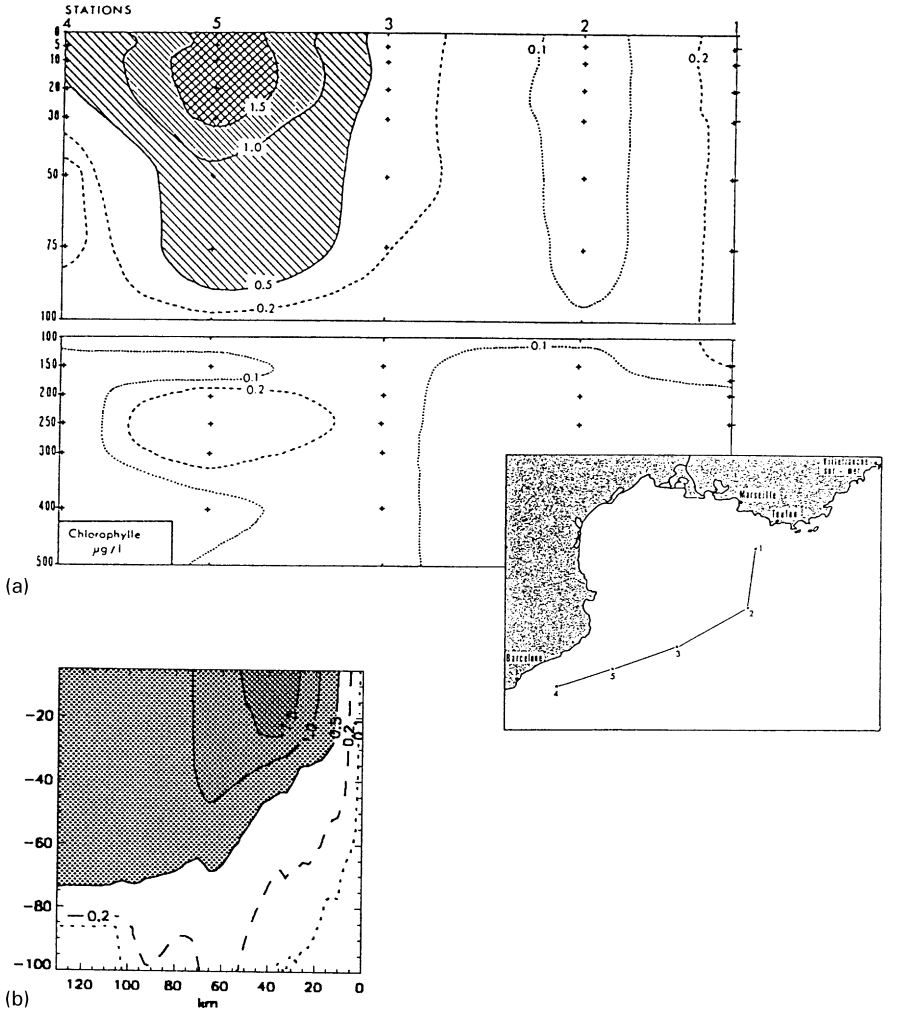

Fig. 11. (a) Chlorophyll vertical distribution along the Toulon-Barcelona transect of Mediprod II (from Nival et al., 1972). The map shows the location of the five stations. (b) Chlorophyll vertical distribution in the model, averaged around the center of the convective area. The *x*-axis shows the distance from the center. Phytoplankton concentrations are converted to chlorophyll using a constant ratio. Because the distance between two stations in the data is approximately 80 km, the horizontal scales are similar in the model and the data figures. This is also the case for the first 100 m of the vertical scale.

symmetry, as we have assumed; it is elongated in the NE-SW direction, which happens to be the Toulon-Barcelona direction, and which can therefore easily explain a discrepancy of factor of two to three. Another supporting figure in the Nival et al. (1972) data is the important sub-surface chlorophyll they observed at station 5. By analyzing the protein and carbohydrate contents of the water column, they found that this

maximum consisted mostly of living cells and attributed it to a downward transport of the cells. The results of our modelling study therefore are in total agreement with their interpretation, as we have shown that mesoscale instabilities can subduct phytoplankton. During the Mediprod I cruises, transects across the MEDOC area were carried out at one month intervals (Coste et al., 1972) in winter and spring. The winter transect shows similar phytoplankton distribution to that of the Mediprod II and of our simulation, with a maximum in phytoplankton at the border of the convective area. In the spring transect, this maximum has moved towards the center (Jacques et al., 1973). Our simulation shows a similar displacement of maximum phytoplankton distribution towards the center with time (Fig. 8) as a response to progressive stratification in the center (Fig. 6).

CZCS observations from 1978 to 1982 (André, 1990; Morel and André, 1991) enable one to follow the mesoscale variability and the annual repetition of the bloom onset: February images show very low surface chlorophyll concentrations in the center of the MEDOC area ($\leqslant 0.05\,\mathrm{mg\,Chl\,m^{-3}}$), where deep convection occurs, and higher concentrations outside ($\sim 0.2\,\mathrm{mg\,Chl\,m^{-3}}$); the boundary of this area can be seen in strong horizontal pigment gradients, meandering with a wavelength varying from 40 to 60 km (Fig. 1). Images from March to May show a global increase of pigment concentrations, and the retraction of pigment-poor water to the center. In May, the mesoscale signature is still present; maximum values of the order of 2–3 $\mathrm{mg\,Chl\,m^{-3}}$ are now found in the center of the area, while minimum values ($\sim 0.2\,\mathrm{mg\,Chl\,m^{-3}}$) are located in the outside area (Fig. 1). These general observations are in agreement with our model results. The February 1981 image is comparable to the simulated surface phytoplankton field at day 16 (Fig. 8): the meandering has the same wavelength, and biomass levels on the center and on the outside are similar. The May 1981 image is comparable to the phytoplankton field at day 36 (Fig. 8): elongated structures of about 100 km length are found in the model as in the data, and maximum values have shifted toward the center as in the data. The value of the maximum in May is underestimated in the model ($\sim 1.5\,\mathrm{mg\,Chl\,m^{-3}}$) compared to CZCS data ($\sim 3-4\,\mathrm{mg\,Chl\,m^{-3}}$). Another failure in the comparison is that none of the CZCS images clearly show a maximum in concentration at the border of the convective area, as our model results and Mediprod measurements seem to suggest. One reason could be that the spatial resolution of these images (about 10 km) is not able to capture this quite narrow band. Other explanations for these discrepancies are the effects of the wind and of the spring warming and are further discussed in the companion paper.

7. Summary and conclusions

The problem that motivated this study was to understand the interactions between mesoscale dynamics and primary production during the onset of a bloom associated with the sinking and spreading phase of a patch of dense water in the MEDOC area. CZCS images over this area and during this period indeed suggested the existence of interactions occurring preferentially at mesoscale. For that purpose, a numerical model was developed. This model links a three-dimensional primitive equation ocean

model to a "NPZD" biogeochemical model. Our model experiments generated mesoscale structures in the phytoplankton field which are correlated to the surface density meanders, and which are similar to those observed by the CZCS sea-color images (André, 1990; Morel and André, 1991). Furthermore, they predicted a maximum of biomass around the convective area, in agreement with field observations (Nival et al., 1972; Jacques et al., 1973). In this situation, the main factor regulating primary production is not nutrient availability, as nutrients brought up to the surface during deep convection are always abundant, but vertical mixing. Therefore, unlike in previous process studies (Flierl and Davis, 1993; Yoshimori and Kishi, 1994; McGillicuddy et al., 1995; Dadou et al., 1996; Smith et al., 1996; McGillycuddy and Robinson, 1997; Spall, 1998), the vertical transport of nutrients to the mixing layer is not fertilizing at that time. Our simulation has enabled us to focus on other mechanisms for mesoscale interactions between primary production and ocean dynamics: when the mixing layer is too deep, vertical movements decrease the time over which cells are exposed to light, and therefore decrease primary production. Mesoscale mixing layer shoaling increases this mean exposure time and thus increases primary production. It has been shown that the majority of phytoplankton production occurs in the trough of the meander, where the mixing layer is the shallowest. Through advection, phytoplankton is then subducted from these source areas towards the crest of the meanders. Therefore, mesoscale processes interfere in two different ways with primary production: first, by modulating the mixing layer depth, and second by rearranging phytoplankton distribution. Our results also suggest that the mesoscale transport of phytoplankton is responsible for a decorrelation between phytoplankton biomass and primary production. In particular, surface phytoplankton concentration, which is the only biological parameter accessible from space, appears to be decorrelated from integrated primary production: the trough of the meanders are twice as productive as the crest, even though the surface phytoplankton concentrations are similar.

Although apparently very specific to a small area in the Mediterranean Sea, the conclusions of this study are very likely to apply on the larger scale. Indeed, in wide regions of the ocean, characterized by deep winter vertical mixing and strong mesoscale activity (part of the North Atlantic and of the Austral ocean), similar mesoscale impacts on primary production through mixing-layer shoaling can be expected. By comparing primary productivity predicted with models of increasing eddy-kinetic energy, Oschlies and Garçon (1998) have estimated mesoscale activity to account for about 40% of primary production in the North of the Atlantic (30°N–65°N). The processes analyzed in this study could explain part of this enhancement. Yet, the spatial and temporal eddy scales explored here are specific to the northwestern Mediterranean Sea conditions. In particular, the restratification time (which controls the production rate of phytoplankton) and the time scale for advection (which explains the decorrelation between productivity and biomass) depend on the width of the convective area and on the Rossby radius of deformation of the ambient fluid (Jones and Marshall, 1997). Work is in progress to investigate similar processes in the case of the North Atlantic.

Acknowledgements

We thank Anne-Marie Tréguier for valuable discussions. We are grateful to C. Lévy and M. Imbard for their help in computing. Funding for this study was provided by the DRET (Direction des Recherches Etudes et Techniques), CNRS (Centre National de la Recherche Scientifique), MATER (MAST program of EEC) and France-JGOFS (Joint Global Ocean Flux Studies). The computer time was provided by the IDRIS center (Institut du Développement et des Resources en Informatique Scientifique). The manuscript was written when M. Lévy was a post-doctoral fellow at the Lamont Doherty Earth Observatory.

Appendix: the NPZD biogeochemical model

The NPZD primary production model used in this study is a simplified version of the BIOMELL biogeochemical model developed in a one-dimensional vertical framework by Lévy et al. (1998b) for the northwestern Mediterranean seasonal cycle of primary production and export fluxes. The simplification mostly concerns the regeneration and the export pathways. It was made possible by the fact that the simplified model was designed to study the winter and spring periods, when regeneration and exports are weak.

The resulting NPZD model consists of four prognostic variables (instead of ten) expressed in terms of their nitrogen content: nutrients (N), phytoplankton (P), zooplankton (Z) and detritus (D) (Fig. 3). The biogeochemical source/sink budgets for each of the variables are (with model parameters in Table 1):

$$S(N) = -\mu_p L_I L_N P + \mu_z Z + \mu_d D \tag{A.1}$$

$$S(P) = \mu_p L_I L_N P - G_p - m_p P \tag{A.2}$$

$$S(Z) = a_p G_p + a_d G_d - \mu_z Z - m_z Z \tag{A.3}$$

$$S(D) = (1 - a_p) G_p + (1 - a_d) G_d + m_p P + m_z Z - \mu_d D - G_z^d - V_d \partial_z D \tag{A.4}$$

The formulation for phytoplankton growth (i.e. primary production, $\mu_p L_I L_N P$) takes into account nutrient and light limitations. Nutrient limitation has the Michaelis-Menten kinetics ($L_N = N/(N + K_N)$). Light limitation has the Webb et al. (1974) type ($L_I = \gamma_m(1 - e^{-\overline{PAR}/K_{PAR}})$), modulated by a parameterization of Lagrangian production inhibition in situations of deep mixing through a specific coefficient γ_m. γ_m is set to 1 (no limitation) when the mixing layer is shallower than the euphotic layer. In such a case, cells within the mixing layer are assumed to experience a mean photosynthetic available radiation $\overline{PAR}$ over the mixing layer. When the mixing layer becomes deeper than the euphotic layer, γ_m decreases accordingly down to a threshold value of 0.1, and $\overline{PAR}$ is taken as the averaged photosynthetic available radiation over the euphotic layer (computed as the 1% incident light depth). This parameterization has been proposed by André (1990) and yielded encouraging results in the one-dimensional study of Lévy et al. (1998b) in the northwestern Mediterranean Sea. It is

Table 1
Parameters for the NPZD model

Nutrient half-saturation constant	K_n	0.5	mmol m^3
Phytoplankton maximal growth rate	μ_p	2	d^{-1}
Carbon/chlorophyll ratio	R_{c-chl}	55	gC/gChl
Half-saturation constant for light	K_{PAR}	33.33	W/m^2
Phytoplankton mortality rate	m_p	0.03	d^{-1}
Zooplankton maximal grazing rate	g_z	0.75	d^{-1}
Half-saturation constant for grazing	K_z	1	mmol/m^3
Assimilated fraction of phytoplankton	a_p	0.7	
Assimilated fraction of detritus	a_d	0.5	
Excretion rate	μ_z	0.1	d^{-1}
Mortality rate	m_z	0.03	d^{-1}
Threshold for zooplankton losses	$Z_{\min}$	0.015	mmol/m^3
Detritus sedimentation speed	V_d	5	m d^{-1}
Detritus remineralisation rate	μ_d	0.09	d^{-1}
Water absorption in red	λ_{r0}	0.225	m^{-1}
Water absorption in blue	λ_{g0}	0.0232	m^{-1}
Pigments absorption in red	λ_{rp}	0.037	m^{-1} (mgChl/m^3)$^{-l_r}$
Pigments absorption in blue	λ_{gp}	0.074	m^{-1} (mgChl/m^3)$^{-l_g}$
Power law for absorption in red	l_r	0.629	
Power law for absorption in blue	l_g	0.674	
Contribution of chlorophyll to absorbing pigments	R_{pig}	0.7	

based on considerations of the light experienced by the phytoplankton cells during their doubling time, which is a purely lagrangian aspect.

Grazing of phytoplankton and detritus is formulated following Fasham et al. (1990):

$$G_p = g_z Z \frac{P^2}{(P+D)K_z + P^2 + D^2} \tag{A.5}$$

$$G_d = g_z Z \frac{D^2}{(P+D)K_z + P^2 + D^2} \tag{A.6}$$

The other biogeochemical interactions taken into account are phytoplankton mortality, zooplankton mortality and zooplankton excretion (these last two processes are inhibited when zooplankton concentration is below a given threshold), fecal pellet production, detritus sedimentation and detritus remineralization.

The photosynthetic available radiation (PAR) is derived from a light absorption model. Only a fraction of the light field (43%) can be used for photosynthesis. Two different light wavelength are considered. The absorption coefficients depend on the local phytoplankton concentrations:

$$\lambda_r = \lambda_{r0} + \lambda_{rp}\mathrm{Chl}^{l_r} \tag{A.7}$$

$$\lambda_g = \lambda_{g0} + \lambda_{gp}\mathrm{Chl}^{l_g} \tag{A.8}$$

$$Chl = 12PR_{c:n}/R_{pig}R_{c:chl} \tag{A.9}$$

$$PAR_r(z=0) = PAR_g(z=0) = 0{,}43\, Q_{sol}/2 \tag{A.10}$$

$$PAR_r(z) = PAR_r(z - \Delta z)\, e^{-\lambda_r \Delta z} \tag{A.11}$$

$$PAR_g(z) = PAR_g(z - \Delta z)\, e^{-\lambda_g \Delta z} \tag{A.12}$$

$$PAR(z) = PAR_r(z) + PAR_g(z) \tag{A.13}$$

The equations for the biogeochemical model are solved for the uppermost 12 model levels ($\sim$200 m). Below, the three biogenic compartments decay to nutrients, with a decaying rate varying from one to 20 days.

References

André, J.-M., 1990. Télédétection spatiale de la couleur de la mer: algorithme d'inversion des mesures du Coastal Zone Color Scanner. Applications à l'étude de la Méditerranée occidentale. Ph.D. Thesis, University Paris 6, France.

Blanke, B., Delecluse, P., 1993. Variability of the tropical Atlantic Ocean simulated by a general circulation model with two different mixed-layer physics. Journal of Physical Oceanography 23, 1363–1388.

Blanke, B., Raynaud, S., 1997. Kinematics of the Pacific equatorial undercurrent: an eulerian and lagrangian approach from GCM results. Journal of Physical Oceanography 27, 1038–1053.

Coste, B., Gostan, J., Minas, H.J., 1972. Influence des conditions hivernales sur les productions phyto et zooplanctoniques en Méditerranée Nord-Ocidentale. I: Structures hydrologiques et distribution de sels nutritifs. Marine Biology 18, 320–348.

Dadou, I., Garçon, V., Andersen, V., Flierl, G., Davis, C., 1996. Impact of the North Equatorial Current meandering on a pelagic ecosystem: a modeling approach. Journal of Marine Research 54, 311–342.

Delecluse, P., Madec, G., Imbard, M., Levy, C., 1993. OPA release 7 Ocean general circulation model. Internal Report LODYC, Université Paris 6, France.

Fasham, M.J.R., Ducklow, H.W., McKelvie, S.M., 1990. A nitrogen-based model of plankton dynamics in the oceanic mixed layer. Journal of Marine Research 48, 591–639.

Flierl, G., Davis, C.S. 1993. Biological effects of Gulf Stream meandering. Journal of Marine Research 51, 529–560.

Gaillard, F., Desaubies, Y., Send, U., Schott, F., 1997. A four-dimentional analysis of the thermal structure in the Gulf of Lion. Journal of Physical Oceanography 102, 12,515–12,537.

Gascard, J.C., 1978. Mediterranean deep water formation, baroclinic instability and oceanic eddies. Oceanologica Acta 1, 315–330.

Jacques, G., Minas, H.J., Minas, M., Nival, P., 1973. Influence des conditions hivernales sur les productions phyto et zooplanctoniques en Méditerranée Nord-Occidentale. II: Biomasse et production phytoplanctonique. Marine Biology 23, 251–265.

Jones, H., Marshall, J., 1997. Restratification after deep convection. Journal of Physical Oceanography 27, 2276–2287.

Killworth, P.D., 1976. The mixing and spreading phases of Medoc I. Progress Oceanography 7(2), 59–90.

Klein, P., Hua, B.L., 1988. Mesoscale heterogeneity of the wind-driven mixed layer: influence of a quasigeostrophic flow. Journal of Marine Research 46, 495–525.

Leaman, K.D., Schott, F.A., 1987. Hydrographic structure of the convection regime in the gulf of Lions: winter 1987. Journal of Physical Oceanography 1:21, 575–598.

Lévy, M., Mémery, L., Madec, G., 1998a. The onset of a bloom after deep winter convection in the North Western Mediterranean sea: mesoscale process study with a primitive equation model. Journal of Marine System, 16, 7–21.

Lévy, M., Mémery, L., André, J.-M., 1998b. New, total and exported productions in the NW Mediterranean Sea: a modelling approach. Journal of Marine Research 56, 197–238.

Madec, G., Chartier, M., Delecluse, P., Crépon, M., 1991a. A three-dimentional numerical study of deep water formation in the northwestern mediterranean sea. Journal of Physical Oceanography 21, 1349–1371.

Madec, G., Chartier, M., Crépon, M., 1991b. The effect of thermohaline forcing variability on deep water formation in the Northwestern Mediterranean Sea: a hight resolution three-dimentional numerical study. Dynamics of Atmospheres and Oceans 15, 301–332.

McGillicuddy, D.J., Robinson, A.R., 1997. Eddy induced nutrient supply and new production in the Sargasso Sea. Deep-Sea Research I 44, 1427–1449.

McGillicuddy, D.J., Robinson, A.R., McCarhy, J.J., 1995. Coupled physical and biological modelling of the spring bloom in the North Atlantic (II): three dimentional bloom and post-bloom processes. Deep-Sea Research I 42, 1359–1398.

Medoc group, 1970. Observation of formation of deep water in the Mediterranean sea, 1969. Nature 227, 1037–1040.

Moisan, J.R., Hofman, E.E., Haidvogel, D.B., 1996. Modeling nutrient and phytoplankton processes in the California coastal transition zone. 2. A three-dimentional physical-bio-optical model. Journal of Geophysical Research 101, 22,677–22,691.

Morel, A. and J.-M. André, 1991. Pigment distribution and primary production in the western Mediterranean as derived and modeled from Coastal Zone Color Scanner observations. Journal of Geophysical Research 96, 12,685–12,698.

Nival, P., Malara, G., Charra, R., Boucher, D., 1972. La matière organique particulaire en Méditerranée occidentale en mars 1970 (chlorophylle, protéines, glucides). Mission "Médiprod II" du Jean-Charcot. Annales de lInstitut Oceanographique 48, 141–156.

Nival, P., Nival, S., Thiriot, A., 1975. Influence des conditions hivernales sur les productions phyto- et zooplanctoniques en Méditerranée nord-occidentale. V: Biomasse et production zooplanctonique – relations phyto-zooplancton. Marine Biology 31, 249–270.

Oschlies, A., Garçon, V., 1998. Eddy-induced enhancement of primary production in a model of the North Atlantic Ocean. Nature 394, 266–269.

Pedlosky, J., 1987. Geophysical Fluid Dynamics, 2nd ed. Springer, Berlin, New York, pp. 490–623.

Pollard, R.T., Regier, L., 1990. Large variations in potential vorticity at small spatial scales in the upper ocean. Nature 348, 227–229.

Riley, G.A., 1942. The relationship of vertical turbulence and spring diatom flowerings. Journal of Marine Research 5, 67–87.

Robinson, A.R., McGillicuddy, D.J., Calman, J., Ducklow, H.W., Fasham, M.J.R., Hoge, F.E., Leslie, W.G., McCarthy, J.J., Podewski, S., Porter, D.L., Saure, G., Yoder, J.A., 1993. Mesoscale and upper ocean variabilities during the 1989 JGOFS bloom study. Deep-Sea Research II 40, 9–35.

Smith, C.L., Richards, K.J., Fasham, M.J.R., 1996. The impact of mesoscale eddies on plankton dynamics in the upper ocean. Deep-Sea Research I 43, 1807–1832.

Smolarkiewicz, K.P., Clark, T.L., 1986. The multidimensional positive definite advection transport algorithm: further development and applications. Journal of Computational Physics 67, 396–438.

Sverdrup, H.U., 1953. On Conditions for the Vernal Blooming of Phytoplankton. Journal of Cons. Int. Expor. Mer. 18, 287–295.

Spall, S.A., 1998. The impact of mesoscale jet activity on plankton heterogenity and primary production; a numerical modelling study. Ph.D. Thesis, University of Southampton.

Watson, A.J., Robinson, C., Robinson, J.E., Williams, P.J.l.B., Fasham, M.J.R., 1991. Spatial variability in the sink for atmospheric carbon dioxide in the North Atlantic. Nature 350, 50–53.

Webb, W.L., Newton, M., Starr, D., 1974. Carbon dioxide exchange of Alnus Rubra: a mathematical model. Ecologia 17, 281–291.

Yoder, J.A., Aiken, J., Swift, R.N., Hoge, F.E., Stegmann, P.M., 1993. Spatial variability in near-surface chlorophyll a fluorescence measured by the Airbone Oceanographic Lidar (AOL). Deep-Sea Research II 40, 33–53.